Arch. Metall. Mater. **68** (2023), 1, 31-36

DOI: https://doi.org/10.24425/amm.2023.141468

YAQIONG GE[1*], ZEXIN CHANG[1], WENXIAN WANG[1], QINGLING HOU[1]

MICROSTRUCTURE AND MICROMECHANICAL BEHAVIORS OF BULK AMORPHOUS ALLOY PREPARED BY SPARK PLASMA SINTERING

This study aimed to prepare Zr55Cu30Al10Ni5 bulk amorphous alloys by spark plasma sintering of raw amorphous alloy powders and investigate their microstructure and micromechanical behaviors. When the sintering temperature (T_s) was 675K, which was lower than the glass transition temperature (T_g) of the material, the sintered sample was almost fully amorphous but the density was lower. However, when T_s was 705K, which was higher than T_g, partial crystallization occurred, but the density was higher. The hardness of the bonding zone of the sintered sample at 675K was 5.291 GPa due to the lower density, which was lower than that at 705K, and the hardness at 705K was 8.836 GPa. The generation of thermodynamically stable intermetallic phases, the hardness, and the elastic modulus of the samples sintered above T_g were higher due to the higher density.

Keywords: Bulk amorphous alloy; Spark plasma sintering; Microstructure; Micromechanical behaviors

1. Introduction

Amorphous alloy is a new metallic functional material with a long-range disorder of atomic structure and without dislocation, grain boundary, phase boundary, and other crystal defects [1,2]. It has better electromagnetic properties, corrosion resistance, and wear resistance than traditional crystalline alloys [3,4]. As a new structural material or functional material, its development has attracted much attention and has a great impact on social development [5].

Under conventional cooling conditions, the melted alloy needs to be cooled at least at a cooling rate of more than 10^5 K/s to prepare a thin banded amorphous alloy with a thickness of tens to hundreds of microns. At present, the traditional methods of preparing amorphous alloys, such as copper mold casting, spray suction casting, strip throwing and water quenching, and so on, cannot break through the critical size limit due to the limited cooling rate [6,7]. The amorphous alloys prepared by them cannot meet the requirements of larger structural or functional parts. Laser 3D printing technology can prepare large-sized bulk amorphous alloys due to the advantages of "layered manufacturing and layer-by-layer superimposition." [8]. However, crystallization can easily occur due to the multiple thermal effects in the process of laser 3D printing, resulting in the low amorphous rate of bulk amorphous alloys, which affects the overall performance of bulk amorphous alloys [9,10].

Spark plasma sintering (SPS) is a new powder metallurgy preparation technology, and the Joule heat is generated at the moment when pulse electric energy and pulse pressure act on the powder to realize the sintering process. It has the advantages of high heating speed, low sintering temperature (T_s), short sintering time, and no size limit [11]. Therefore, SPS is one of the effective methods to break through the critical size of bulk amorphous alloy and avoid crystallization effectively. However, T_s is one of the important factors affecting the preparation of bulk amorphous alloys by SPS. A certain gap still exists between the mechanical properties of amorphous alloys prepared by this technology and those of as-cast samples [12-15].

In this study, bulk amorphous alloys were prepared by SPS technology at two different temperatures, which were lower than and higher than the glass transition temperature (T_g) separately. The nanoindentation behavior of the prepared bulk amorphous alloy and the relationship between the nanoindentation behavior and the sintering process and microstructure were studied. Moreover, the effect of T_s and the bonding zone on the micromechanical behavior of the sintered bulk amorphous alloys was also discussed.

[1] TAIYUAN UNIVERSITY OF SCIENCE AND TECHNOLOGY, COLLEGE OF MATERIALS SCIENCE AND ENGINEERING, TAIYUAN 030024, CHINA

* Corresponding author: geyaqiong@tyust.edu.cn

2.Experiment

2.1. Materials

The amorphous alloy powders with a nominal composition of Zr55Cu30Al10Ni5 prepared by gas atomization were used as the original material for this experiment. The preparation process of powders was as follows. First, the Zr55Cu30Al10Ni5 alloy ingot was prepared by the arc melting method, and then the alloy ingot was remelted by induction heating in a vacuum quartz tube to form a liquid alloy. Then, the liquid alloy was injected into the nozzle and atomized by high-pressure helium; therefore, Zr55Cu30Al10Ni5 amorphous powders with particle size ranging from 10 μm to 100 μm were obtained. Finally, the prepared Zr55Cu30Al10Ni5 amorphous powders were stored in a vacuum glove box to avoid oxidation and pollution. The preparation processing of the original amorphous powders is shown in Fig. 1.

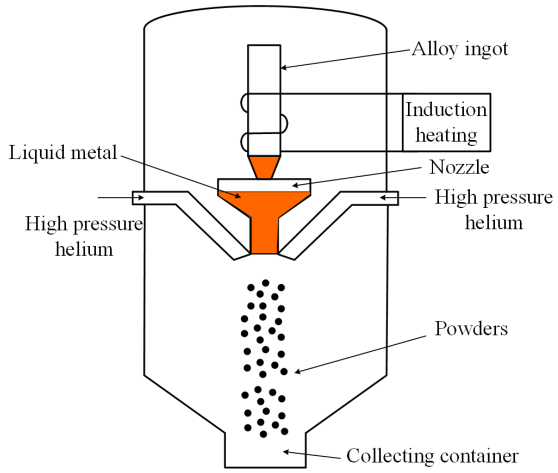

Fig. 1. Preparation processing diagram of original amorphous powders

2.2. Preprocessing

The raw amorphous powders were sintered in a vacuum using the SPS-331lx sintering equipment. A thermocouple inserted into the graphite mold wall of the sintering equipment at a position about 2 mm away from the sintered sample was used to measure and control the T_s. During sintering, vertical pressure was applied to the sintered sample.

The amorphous structure was metastable, and the lower the T_s, the better it was to avoid the crystallization of amorphous. In this experiment, two temperatures near T_g were selected as the T_s, which were 675 K and 705 K. In the initial stage of sintering, the alloy was heated to T_s – 50K at the rate of 80 K/min. When the temperature was between T_s – 50 K and T_s, the heating rate was 30 K/min. When the temperature reached T_s, the alloy remained warm for 5 min, and then cooled down naturally. The sintering pressure was 60 MPa during sintering. The sintering process and the sintered sample are shown in Fig. 2. The final sintered sample prepared by SPS was a cylindrical sample with a diameter of 20 mm and a height of 5 mm.

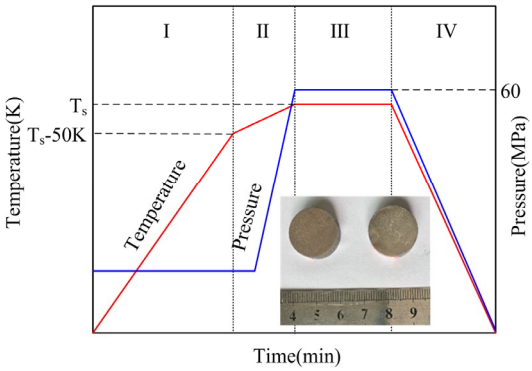

Fig. 2. The SPS processing and the cylindrical amorphous alloy sample prepared by SPS

2.3. Characterization

An x-ray diffractometer(XRD, td-3500, Cu Kα) was used to test the phase structures of raw powders and sintered samples. The diffraction angle was $2\theta = 20°$-$80°$, and the diffraction step was 0.02°. The differential scanning calorimetry (DSC, TA-Q2000) was used to test the thermal properties of raw powders and the sintered samples. The heating rate was 0.50 K/s. A JEOL scanning electron microscope(SEM, JSM-7001F) was used to observe the microstructures of the raw powders and the sintered samples, and the nanoindentation morphology. An Agilent G200 Tribo Indenter with a Berkovich diamond tip was used to test the nanoindentation behaviors of the sintered samples. The maximum load was 120 mN, and the constant loading and unloading rate was 1.0 mN/s.

3. Results and discussion

3.1. Raw powders

The scanning electron microscope image of the raw amorphous powders shown in Fig. 3a indicated that the powders were almost smooth spheres and the size of the particles ranged from 10 μm to 100 μm. The phase structure characteristics of the powders used in this experiment are shown in Fig. 3b. The figure shows only a wide diffraction peak, indicating that the powders were complete amorphous structures. As shown in Fig. 3c, the raw powders were amorphous. Fig. 3c shows that T_g of the powders was about 685K, and the crystallization starting temperature (T_x) was about 762K.

3.2. Microstructure

Fig. 4 shows the x-ray diffraction (XRD) patterns of original amorphous powders and bulk amorphous alloy prepared by SPS at different T_s temperatures. When the T_s was 675K ($<T_g$), the XRD pattern of the bulk amorphous alloy obtained at this temperature was generally consistent with that of the initial

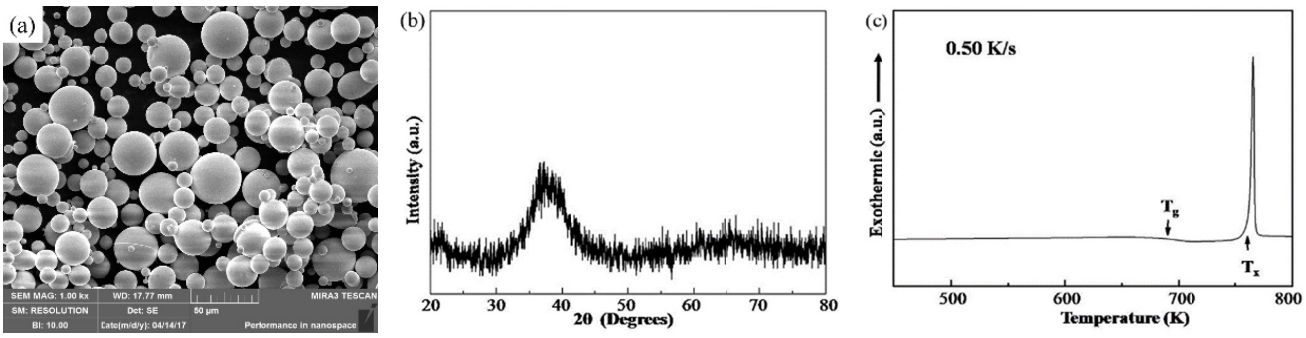

Fig. 3. (a) Scanning electron micrograph; (b) XRD pattern; (c) DSC curve of the raw Zr55Cu30Al10Ni5 amorphous powders

amorphous alloy powders. It was a diffraction curve with wide halo characteristics, and no crystal peak was observed, indicating that the bulk amorphous obtained at this temperature was almost completely amorphous. When the T_s was 705K ($>T_g$), the main diffraction peak of the XRD curve of the bulk amorphous was narrower and the peak shape was wider, indicating that crystallization occurred. The crystallization peak also showed that Cuo, ZrCu, and $Ni_{10}Zr_7$ was formed in the amorphous matrix. Therefore, when the T_s was lower than T_g, it was easier to obtain an amorphous alloy in a completely amorphous state.

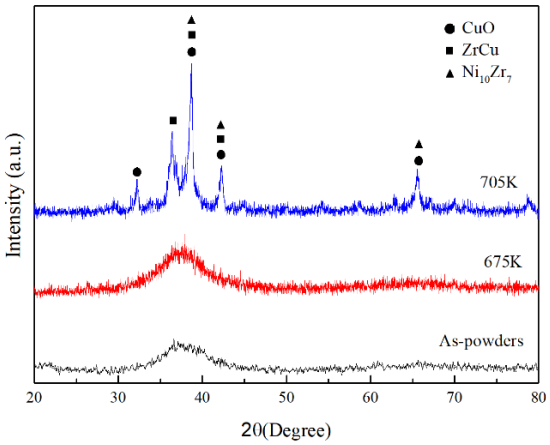

Fig. 4. XRD patterns of the raw Zr55Cu30Al10Ni5 powders and sintered samples at different T_s

According to some studies, the T_s of amorphous materials should be in the supercooled liquid region [13,15]. The difference was that although the T_s of 705K in this test was within the temperature range of the supercooled liquid region of amorphous materials, crystallization still occurred. This was due to the special heat generation mechanism of SPS. During SPS sintering, the heat was generated directly from the interior of the sintering system, resulting in the temperature of the mold being lower than that of the internal sample, while the thermocouple of SPS sintering equipment could only measure the temperature of the mold. Therefore, when the T_s was 705K, the temperature of the sample was higher than the setting T_s, even beyond the initial crystallization temperature(T_x), resulting in crystallization.

The microstructure of the samples was studied, as shown in Fig. 5. When sintering at 675K and 705K, the powders were connected. On the one hand, in the early stage of SPS, the surface of powders was impacted by positive ions and electrons moving at high speed in the electric field, and consequently the oxide layer, impurities, and gas were damaged. The surface of the particles was activated, which promoted material diffusion. Therefore, the sintering time and T_s were shortened. On the other hand, Joule heat was generated at the contact part of the powders under the action of the current, which made the edge of the powders melt locally. At the same time, under the action of the external load, the powders were bonded together to form a sintering neck, and the powders were gradually densified to form a block alloy sample.

For the sample sintered at 675K, the original independent powders were combined. The initial morphology of powders was not oblivious, but the sintered block was not welded tightly, and a small number of holes still existed. Sintering at this temperature, the densification of the sample was attributed to the local plastic deformation of the powders because the temperature did not rise to T_g. When T_s increased to 705K, which was higher than T_g, the sintered sample was more compact. The powders underwent viscous flow deformation under external pressure, the pores between the particles were filled, and the density increased because this temperature entered the supercooled liquid region. Although denser bulk amorphous alloys could be obtained by sintering at a temperature greater than T_g, the degree of amorphous density reduced.

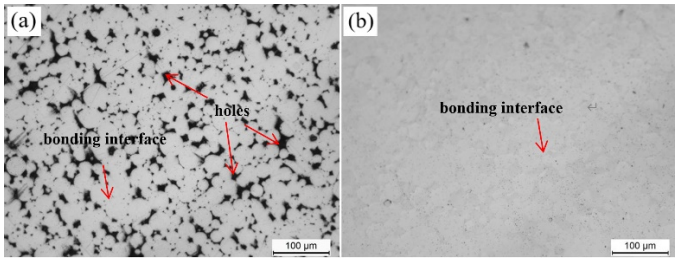

Fig. 5. Microstructures of the bulk Zr55Cu30Al10Ni5 amorphous alloy sintered at different temperatures: (a) 675K, (b) 705K

3.3. Nanoindentation results

Fig. 6 shows the P–h curves tested by nanoindentation tests of the bulk Zr55Cu30Al10Ni5 samples sintered at 675K

at various testing positions(X1, X2, X3, X4 and X5). Although some pores were found in the bulk amorphous alloy sintered at 675K, resulting in low density and incomplete connection, these nanoindentation test points were located in the interior of the particles and at the bonding interface between powder particles, which could reflect the micromechanical behavior of the bulk amorphous alloy at this temperature to a certain extent. The loading curves of X1, X2, X4 and X5 basically coincided, indicating that the composition and structure of other regions of the sample were relatively uniform, except the binding zone (X3). As indicated by the arrows in Fig. 6, similar serrated patterns were found in the P–h curves at all testing positions of the bulk amorphous sample sintered at T_s = 675K, and the formation of these serrated patterns was usually referred to as the "pop-in" events [16,17]. During the nanoindentation tests, a large number of shear bands were activated at the test position due to the action of the indenter pressed on the test position. The formed shear bands continued to propagate due to the continuous press of the indenter, resulting in the "pop-in" events. The P–h curve at the bonding interface (X3) of powder particles moved to the right as a whole. The indentation size in this zone was significantly larger and deeper than that at other positions(X1, X2, X4 and X5). This might be because the hardness of the bonding zone was lower than that in other zones.

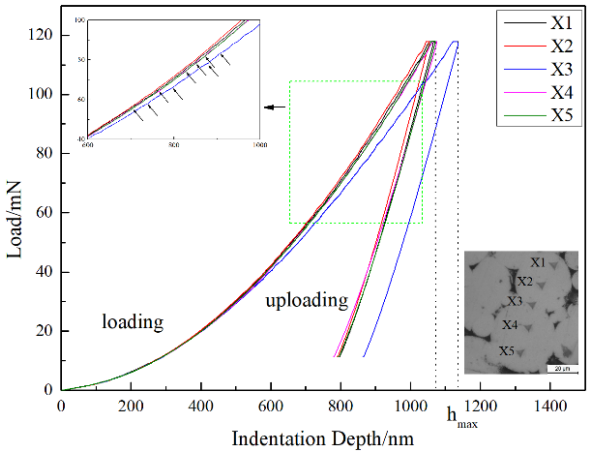

Fig. 6. P–h curves of bulk Zr55Cu30Al10Ni5 amorphous alloy samples sintered at 675 K

Fig. 7 shows the P–h curves tested by nanoindentation tests of the bulk Zr55Cu30Al10Ni5 amorphous alloy samples sintered at 705K at various testing positions(S1, S2, S3, S4 and S5). The loading curves at all positions basically coincided, indicating that the composition and structure of the sample sintered at 705K were relatively uniform. Moreover, few serrations were observed in the P–h curves of T_s = 705K. This might be because partial crystallization occurred when T_s = 705K, which was higher than T_g, and this corresponded to the results shown in Fig. 4.

The indentation morphology of the two samples was observed to further explore the nanomechanical behavior of samples sintered below and above T_g, as shown in Fig. 8. Obvious multiple circular rings existed around the triangular indentation

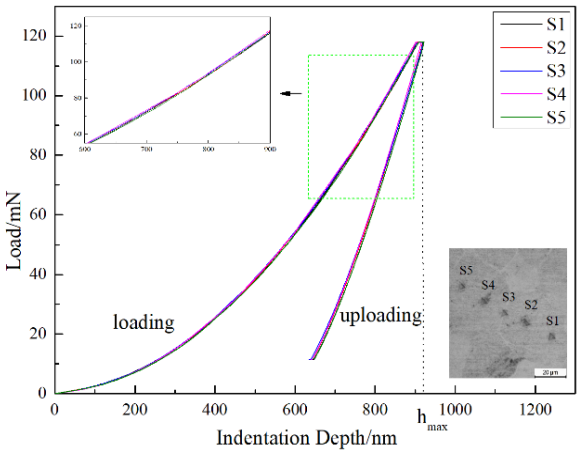

Fig. 7. P–h curves of bulk Zr55Cu30Al10Ni5 amorphous alloy samples sintered at 705K

in the sample sintered at 675K, as shown in Fig. 8a, that is, shear bands. According to previous studies [16-18], this indicated that discrete shear bands were formed around the indenter, which meant that the plastic deformation of the sample was highly locally concentrated. In the case of the sample sintered at 705K, few distinct features were observed, as shown in Fig. 8b. This might be due to the higher density and higher hardness of the sample underneath the indenter.

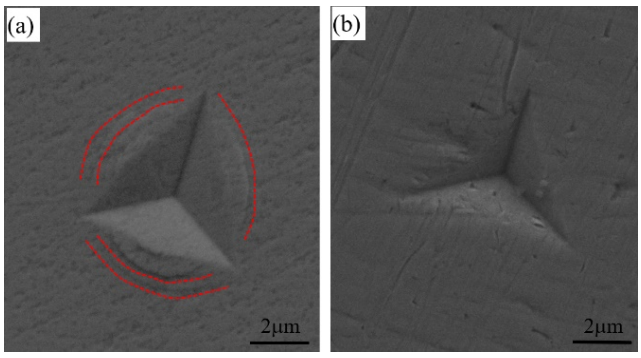

Fig. 8. Indentation morphology of the bulk Zr55Cu30Al10Ni5 amorphous alloy sintered at different temperatures: (a) 675K, (b) 705K

Fig. 9 shows the hardness and elastic modulus of Zr-55Cu30Al10Ni5 samples sintered at 675K and 705K at different testing positions; they are listed in TABLE 1. As shown in Fig. 9a, as $T_s < T_g$, the hardness and elastic modulus of bulk Zr55Cu30Al10Ni5 amorphous alloy at X3 were significantly lower than those at other positions(X1, X2, X4 and X5). This was due to the local melting of the particle edge during SPS. The particles bonded to each other under the action of the external load; therefore, microcrystallization occurred at the junction of powder particles. The generation of microcrystallization led to the hardness and elastic modulus of this bonding zone being lower than that of other amorphous zones. The hardness and modulus of each testing point (S1, S2, S3, S4 and S5) of the sintered sample at 705K were almost the same, which might be due to the overall crystallization of the sample during sinter-

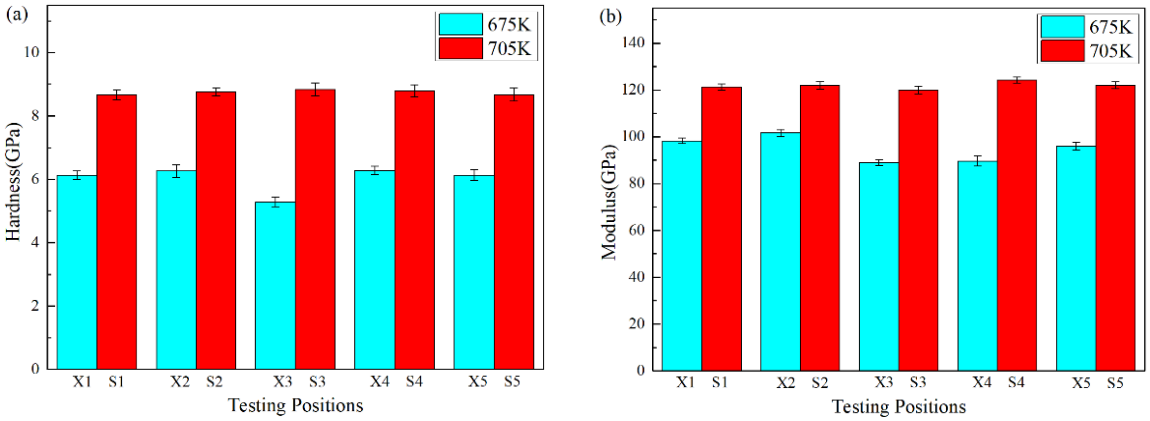

Fig. 9. (a) Hardness and (b) elastic modulus of bulk Zr55Cu30Al10Ni5 amorphous alloy samples sintered at different temperatures

TABLE 1

Nanoindentation data of bulk Zr55Cu30Al10Ni5 amorphous alloy sintered at different temperatures

Sintering temperature	**675K**			**705K**		
Testing positions	**Hardness H_n (GPa)**	**Modulus E (GPa)**	**h_{max} (nm)**	**Hardness H_n (GPa)**	**Modulus E (GPa)**	**h_{max} (nm)**
X1(S1)	6.130	98.220	1063.007	8.666	121.242	918.346
X2(S2)	6.262	101.682	1051.144	8.755	121.961	915.68
X3(S3)	5.291	89.037	1135.167	8.836	120.066	917.051
X4(S4)	6.282	89.590	1073.070	8.795	124.308	912.500
X5(S5)	6.134	95.950	1068.509	8.678	122.03	919.378

ing at 705K, corresponding to Fig. 4. Moreover, the hardness and modulus of the samples sintered at 705K were higher than those of samples sintered at 675K because the compactness of the samples sintered at 705K was higher than that at 675K. In addition, the nanohardness (H_n) decreased with the increase in the maximal indentation depth (h_{max}), as shown in TABLE 1.

4. Conclusions

In this study, bulk amorphous alloys were successfully prepared by SPS of raw amorphous alloy powders at lower temperatures, which were 675K ($<T_g$) and 705K ($>T_g$), respectively. The microstructure and micromechanical behaviors of the bulk amorphous alloys were investigated.

(1) At a sintering temperature (T_s = 675K) below T_g (685K), the Zr55Cu30Al10Ni5 bulk amorphous alloy with a higher degree of amorphization was fabricated by SPS. However, at 705K, which was higher than T_g, the obtained bulk alloy was crystallized.

(2) Under the combined action of electric field, temperature, and pressure of the SPS sintering process, the edge of powder particles melted to form the sintering neck, and bulk alloy was obtained finally. When the T_s was 675K, a certain number of pores were observed in the sintered block, and the density was lower. When the T_s was 705K, the compactness of the sintered block was higher due to viscous flow deformation.

(3) Obvious shear bands and "pop-in" were noted in the nanoindentations in the interior of the particles and at the junction of the metallurgically bonded particles of the sintered bulk amorphous alloy at 675K. The toughness and overall hardness of the sample were good, but the hardness of the bonding zone was lower, which was 5.291 GPa.

(4) The hardness and modulus of the bulk amorphous alloy sintered at 705K were uniform and relatively higher due to the uniform overall structure formed by crystallization and densification.

Acknowledgments

This project was supported by Supported by Fundamental Research Program of Shanxi Province (No.202103021224266, No.202103021223297), Shanxi Scholarship Council of China (No. 2021-139) and Scientific and Technological Innovation Programs of Higher Education Institutions in Shanxi (No. 2021L307).

REFERENCES

[1] C. Zhang, D. Ouyang, S. Pauly, L. Liu, 3D printing of bulk metallic glasses, Mater. Sci. Eng. R. **145**, 100625 (2021). DOI: https://doi.org/10.1016/j.mser.2021.100625

[2] A. Inoue, A. Takeuchi, Recent development and application products of bulk glassy alloys, Acta Mater. **59**, 2243-2267 (2011). DOI:10.1111/j.2041-1294.2010.00019.x

[3] C. Zhang, X.M. Li, S.Q. Liu, et al., 3D printing of Zr-based bulk metallic glasses and components for potential biomedical applications, J. Alloys Comp. **790**, 963-973 (2019). DOI: https://doi.org/10.1016/j.jallcom.2019.03.275

[4] M.F. Ashby, A.L. Greer, Metallic glasses as structural materials, Scr. Mater. **54**, 321-326 (2006). DOI: https://doi.org/10.1016/j.scriptamat.2005.09.051

[5] W.H. Wang, Development and implication enlightenment of amorphous alloys, Bull. Chin. Acad. Sci. **37**, (2022). DOI: https://doi.org/10.16418/ j.issn.1000-3045.20211208008

[6] Z.X. Chang, Y.Q. Ge, L. Sun, et al., The micro-zones formation of Zr-based bulk metallic glass composite fabricated by laser 3D printing, J. Manuf. Process. **76**, 167-174 (2022). DOI: https://doi.org/10.17265/2161-6221/2017.7-8.001

[7] Q.S. Zhang, W. Zhang, A. Inoue, Preparation of Cu36Zr48Ag8Al8 bulk metallic glass with a diameter of 25mm by copper mold casting, Mater. Trans. **48**, 629-631 (2007). DOI: https://doi.org/10.2320/matertrans.48.629

[8] M.M. Prabhakar, A.K. Saravanan, A. Haiter Lenin, et al., A short review on 3D printing methods, process parameters and materials, Mater. Today: Proc. **45**, 6108-6114 (2021). DOI: https://doi.org/10.1016/j.matpr.2020.10.225

[9] Y.Q. Ge, X. Chen, Z.X. Chang, The forming and crystallization behaviors of $Zr_{50}Ti_5Cu_{27}Ni_{10}Al_8$ bulk amorphous alloy by laser additive manufacturing, Mater. Express. **10**, 1155-1160 (2020). DOI: https://doi.org/10.1166/mex.2020.1724

[10] O.Y. Di, P.C. Zhang, C. Zhang, et al., Understanding of crystallization behaviors in laser 3D printing of bulk metallic glasses, Appl. Mater. Today. **23**, 100988 (2021). DOI: https://doi.org/10.1016/j.apmt.2021.100988

[11] C.K. Zhuang, H.P Ding, Y.F Ma, et al., Research progress of preparation of amorphous alloys via spark plasma sintering, Rare Metal Mater. Eng. **50**, 1096-1106(2021).

[12] Q. Li, G. Wang, X.P. Song, et al., Ti50Cu23Ni20Sn7 bulk metallic glasses prepared by mechanical alloying and spark plasma sintering, J. Mater. Process. Technol. **209**, 3285-3290 (2009). DOI: https://doi.org/10.1016/j.jmatprotec.2008.07.050

[13] Z.H. Chu, H. Kato, G.Q. Xie, et al., Consolidation and mechanical properties of Cu46Zr42Al7Y5 metallic glass by spark plasma sintering, J. Non Cryst. Solids. **358**, 1263-1267 (2012). DOI: https://doi.org/10.1016/j.jnoncrysol.2012.02.027

[14] X.P. Li, M. Yan, H. Imai, et al., Fabrication of 10mm diameter fully dense Al86Ni6Y4.5Co2La1.5 bulk metallic glass with high fracture strength, Mater. Sci. Eng. A. **568**, 155-159 (2013). DOI: https://doi.org/10.1016/j.msea.2013.01.04l

[15] L.L. Ji, X.B. Yun, Y.Z. Lü, et al., Preparation of Zr50Ti5Cu27Ni10Al8 bulk amorphous alloy by spark plasma sintering, Chin. J. Rare Met. **44**, 1221-1226 (2020). DOI: info:doi/10.1166/mex.2020.1724

[16] C.A. Schuh, T.G. Nieh, A nanoindentation study of serrated flow in bulk metallic glasses, Acta Mater. **51**, 87-99 (2003). DOI: https://doi.org/10.1016/S1359-6454(02)00303-8

[17] S. Vincent, B.S. Murty, M.J. Kramer, et al., Micro and nano indentation studies on Zr60Cu10Al15Ni15 bulk metallic glass, Mater. Des. **65**, 98-103 (2015). DOI: https://doi.org/10.1016/j.matdes.2014.09.017

[18] A. Concustell, N. Mattern, H. Wendrock, et al., Mechanical properties of a two-phase amorphous Ni-Nb-Y alloy studied by nanoindentation, Scr. Mater. **56**, 85-88 (2007). DOI: https://doi.org/10.1016/j.scriptamat.2006.09.026

[19] A.L. Greer, A. Castellero, S.V. Madge, et al., Nanoindentation studies of shear banding in fully amorphous and partially devitrified metallic alloys, Mater. Sci. Eng. A. **375-377**, 1182-1185 (2004). DOI: https://doi.org/10.1016/j.msea.2003.10.032